

**PRACTICAL SUPERCONDUCTOR DEVELOPMENT  
FOR ELECTRICAL POWER APPLICATIONS  
ARGONNE NATIONAL LABORATORY  
QUARTERLY REPORT FOR THE PERIOD ENDING JUNE 30, 2001**

This is a multiyear experimental research program focused on improving relevant material properties of high- $T_c$  superconductors (HTSs) and on development of fabrication methods that can be transferred to industry for production of commercial conductors. The development of teaming relationships through agreements with industrial partners is a key element of the Argonne (ANL) program.

### **Technical Highlights**

Recent results are presented on the fabrication and characterization of  $\text{YBa}_2\text{Cu}_3\text{O}_x$  (YBCO)-coated conductors, substrate development, and basic studies of substrate oxidation studies. In applications, the response of a bulk superconductor to a transient magnetic field is described and the implications for fault-current limiters are discussed.

### Fabrication of Coated Conductors

We report here on YBCO films that were grown by pulsed laser deposition (PLD) on biaxially textured yttria-stabilized zirconia (YSZ) that was deposited on Hastelloy C (HC) substrates by ion-beam-assisted deposition (IBAD). It is shown that substrate temperature significantly influences in-plane texture of the YSZ layer and that biaxial alignment of the YSZ layer improves with thickness of the YSZ layer. It is also shown that a thin  $\text{CeO}_2$  buffer layer ( $\approx 10$  nm) improves the lattice match between the YSZ and YBCO films and enhances biaxial alignment of YBCO films.

Mechanically polished HC pieces measuring  $\approx 0.1$  mm thick, 1 cm long, and  $\approx 5$  mm wide were used as substrates for IBAD YSZ and subsequent YBCO deposition. YSZ thin buffer films were grown from sintered YSZ pieces by e-beam evaporator. Polished HC substrates were attached to a water-cooled sample stage with vacuum silver paste. The  $\text{Ar}^+$  ion beam, generated by an 8-cm Kaufman source operating at 300 eV, has an incident angle of  $55^\circ$  with respect to the substrate normal. A Faraday cup (Kimball Physics FC-70A) was used to measure the beam intensity before each deposition. Base pressure of the deposition chamber was  $2 \times 10^{-7}$  torr, and  $\approx 1 \times 10^{-4}$  torr operating pressure was maintained with a flowing 10:1 argon-oxygen mixture and a cryogenic pump. A quartz crystal monitor was mounted beside the sample stage to monitor the deposition rate. Circulating water

was introduced to the sample stage to dissipate heat generated by the ion source and to maintain the substrate temperature below 100°C during the entire deposition. Without the use of cooling water, substrate temperature would rise to  $\geq 250^\circ\text{C}$ .

YBCO films 300 to 1000 nm thick were deposited by PLD with a Lambda Physik COMPex 201 excimer laser; a Kr-F<sub>2</sub> gas premixture was the lasing medium. Commercial YBCO targets (Superconductive Components, Inc., Columbus, OH) of 25.4 mm diameter and 6.4 mm thickness, were used. Substrates were attached to a heatable sample stage with silver paste and heated to  $\approx 800^\circ\text{C}$  during deposition. The laser spot focused at the rotating target was 2-3 mm; this resulted in an energy density of  $\approx 2 \text{ J/cm}^2$ . Distance between the target and the substrates was 7 cm. The desired oxygen partial pressure (in the range of 100-300 mtorr) was obtained by flowing ultra-high-purity oxygen through the chamber. A pulse repetition rate of 8 Hz produced a growth rate of  $\approx 15 \text{ nm/min}$ . To improve the lattice match between YBCO and IBAD YSZ, a  $\approx 10\text{-nm}$ -thick CeO<sub>2</sub> buffer layer was deposited at  $800^\circ\text{C}$  by PLD before depositing YBCO.

The superconducting critical transition temperature ( $T_c$ ) and critical current density ( $J_c$ ) were determined by the inductive method and confirmed by the four-probe transport method at 77 K in liquid nitrogen. The inductive test was used as a standard characterization tool to measure the superconducting properties of our YBCO films. Thin-film superconductor samples were placed between a primary and secondary coil pair with inner diameters of 1 mm and outer diameters of 5 mm. Alternating current was introduced to the primary coil and detected from the secondary coil by a lock-in amplifier (Stanford Research Systems SR830 DSP). Samples used for transport measurements were first coated with 2- $\mu\text{m}$ -thick silver by e-beam evaporation and then annealed in flowing high-purity oxygen at  $400^\circ\text{C}$  for 2 h. Typical samples used for the four-probe transport measurement were 3-5 mm wide and 1 cm long.

Texture was examined by X-ray diffraction pole figure analysis with Cu-K $\alpha$  radiation. In-plane texture was characterized by the full-width-at-half-maximum (FWHM) of  $\phi$ -scans for the YSZ (111) reflection ( $2\theta = 30.1^\circ$ ), while out-of-plane texture was characterized by the FWHM of  $\omega$ -scan for YSZ (002) reflection ( $2\theta = 34.9^\circ$ ). Atomic force microscopy (AFM) observations were conducted with a Digital Instruments D3100 SPM. TEM used a Philips CM30 microscope operated at 300 keV.

Crystalline texture of the IBAD YSZ films was characterized by X-ray diffraction pole figure analysis. Better in-plane alignment in the IBAD YSZ template films helps to reduce the high-angle grain boundaries in YBCO films, and therefore to increase  $J_c$ . A typical YSZ (111) X-ray pole figure is shown in Fig. 1. Four well-defined (111) poles are evenly distributed with respect to azimuth angle and have a tilt (chi angle) of  $\approx 55^\circ$ . This confirmed that the (00l) planes of the IBAD YSZ film are

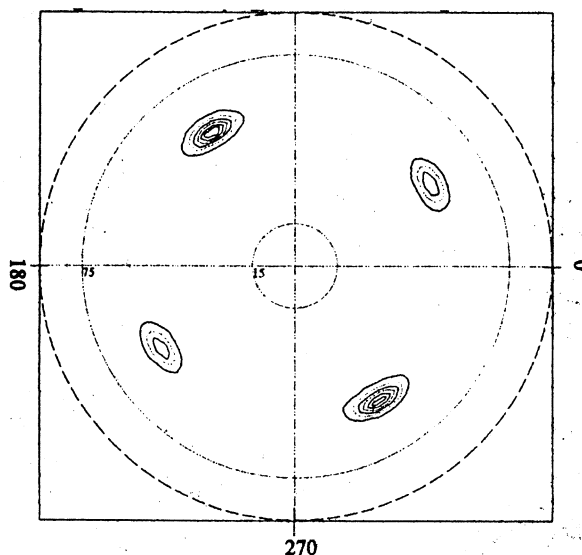


Fig. 1. YSZ (111) pole figure of IBAD YSZ film deposited on HC substrate with 300 eV ion beam energy and at substrate temperature of 90°C.

parallel to the substrate surface. Figures 2 and 3 show YSZ (111)  $\phi$ -scan and  $\omega$ -scan patterns for  $\approx 1 \mu\text{m}$  YSZ films deposited on the HC substrate, respectively. The FWHM of the YSZ (111)  $\phi$ -scan is usually used to quantitatively characterize in-plane textures of IBAD YSZ films. Out-of-plane texture was characterized from YSZ (002)  $\omega$ -scan, as shown in Fig. 3. We obtained YSZ (111)  $\phi$ -scan FWHM of 13.2° and YSZ (200)  $\omega$ -scan FWHM of 7.7° for the IBAD YSZ films deposited with 300 eV beam energy and at a substrate temperature of 90°C.

Figure 4 plots the FWHM of YSZ (111)  $\phi$ -scan vs. the substrate temperature during deposition of  $\approx 1 \mu\text{m}$  thick IBAD YSZ films. In-plane texture of the IBAD YSZ films improved with a decrease in substrate temperature. These results suggest that a FWHM of  $\approx 12^\circ$  could be obtained with a substrate temperature of  $\approx 50^\circ\text{C}$ .

Figure 5 shows a top-surface AFM image of an IBAD YSZ film. A dense, smooth surface with root-mean-square (RMS) roughness of  $\approx 3.3 \text{ nm}$  was observed. Figure 6 shows a cross-sectional TEM image and selected-area diffraction (SAD) patterns of IBAD YSZ at various distances from the substrate. The SAD patterns indicate that biaxial alignment in the YSZ film improves with increasing film thickness; a thickness of 500 to 800  $\mu\text{m}$  is necessary for good in-plane texture in the YSZ films.

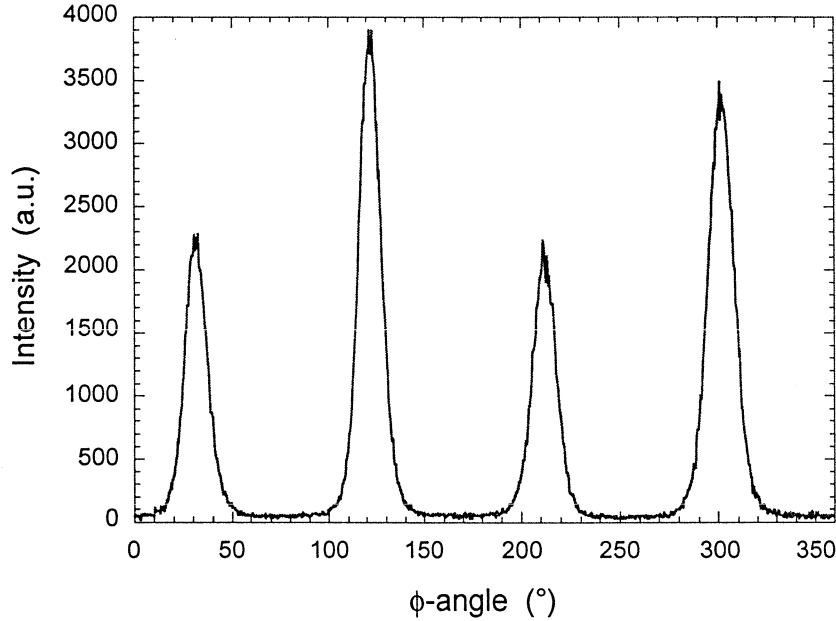


Fig. 2. In-plane texture of IBAD YSZ film deposited on HC substrate with 55° bombardment angle, 300 eV beam energy, and at substrate temperature of 90°C.

Biaxially aligned YBCO films were successfully deposited on IBAD YSZ buffered HC substrates by PLD under the conditions listed in Table 1. An XRD 2 $\theta$ -scan of YBCO directly deposited on HC substrate reveals tiny YBCO (*l*00) peaks, as shown in Fig. 7a. To reduce the lattice mismatch between YBCO and YSZ, a  $\approx$ 10-nm-thick CeO<sub>2</sub> buffer layer was deposited on the YSZ film by e-beam evaporation before PLD of the YBCO. Deposition of the ceria buffer layer on the YSZ film helped to reduce a-axis misalignment and improve c-axis alignment, as shown in Fig. 7b. The YBCO (*l*00) peaks disappeared in the XRD pattern of the sample with the ceria buffer layer. Layer-by-layer XRD  $\phi$ -scans of the sample indicated epitaxial growth of the CeO<sub>2</sub> and YBCO films, as shown in Fig. 8. In-plane texture FWHMs of 12° and 9° were observed for CeO<sub>2</sub> (111) and YBCO (103), respectively.

We obtained  $T_c = 90$  K for a 0.5- $\mu$ m-thick YBCO film deposited on the ceria-buffered IBAD YSZ fabricated on HC substrate. From inductive measurements, Fig. 9 shows that the superconducting transition was completed at 88.5 K. Critical current density for this sample is  $2.2 \times 10^6$  A/cm<sup>2</sup> at 77 K with zero external field.

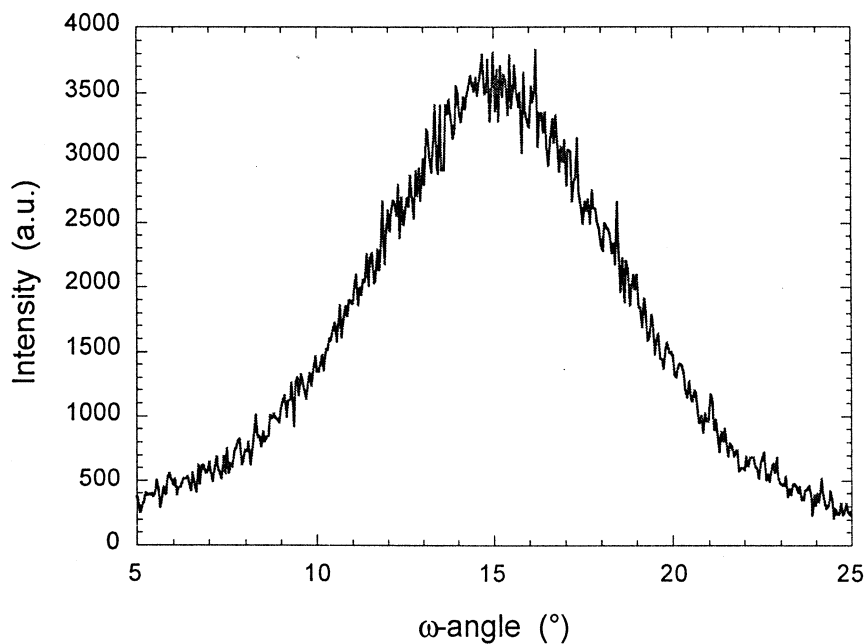


Fig. 3. Out-of-plane texture of IBAD YSZ film deposited on HC substrate with  $55^{\circ}$  bombardment angle, 300 eV beam energy, and at substrate temperature of  $90^{\circ}\text{C}$ .

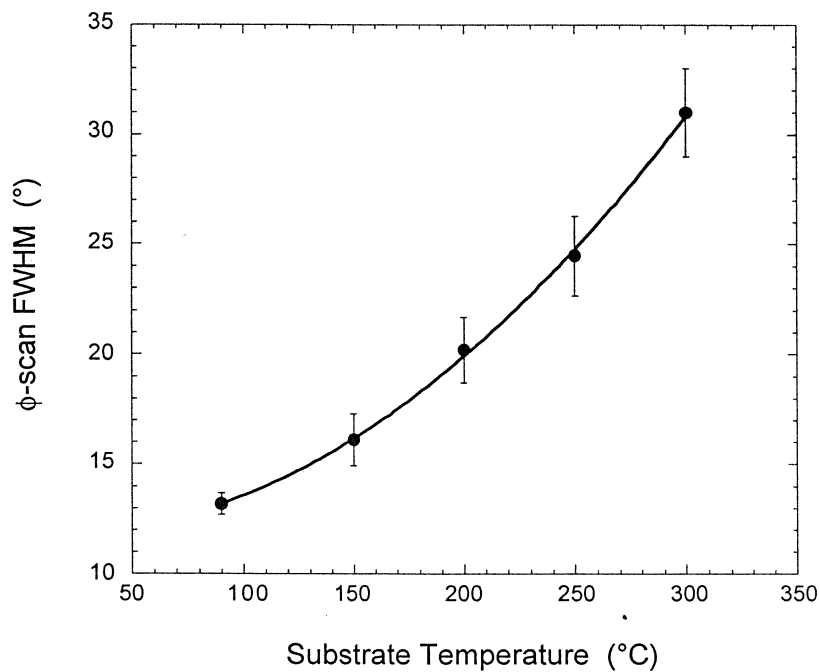


Fig. 4. FWHM of YSZ (111)  $\phi$ -scan for IBAD YSZ films deposited at various substrate temperatures.

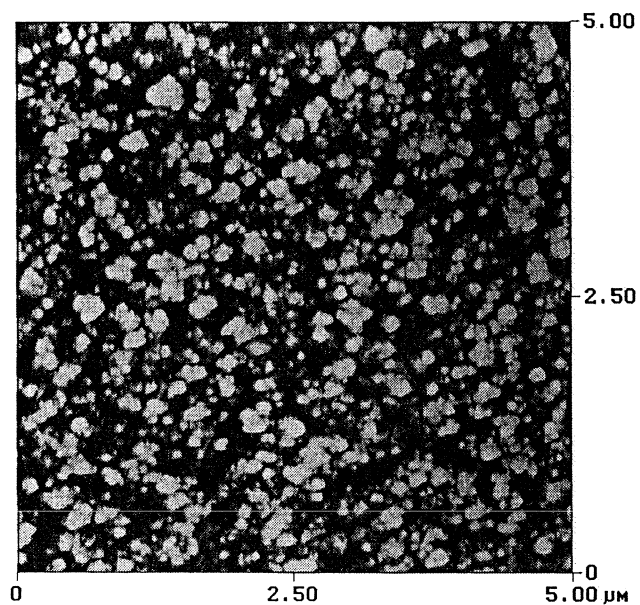


Fig. 5. AFM image of top surface of IBAD YSZ film deposited with 300 eV beam energy at 90°C substrate temperature.

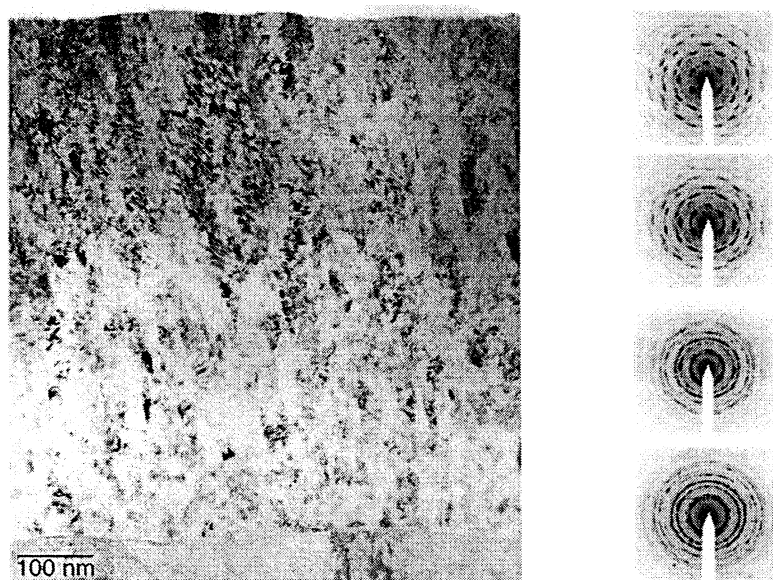


Fig. 6. Cross-sectional TEM and SAD patterns of IBAD YSZ at four distances from the substrate.

Table 1. Conditions used for epitaxial growth of YBCO by PLD

Laser wavelength	248 nm (Kr-F)
Repetition rate	8 Hz
Pulse width	25 ns
Energy density	1-3 J/cm <sup>2</sup>
Substrate temperature	700-800°C
Operating pressure	100-300 mtorr
Oxygen flow rate	10 sccm
Target-to-substrate distance	4-8 cm

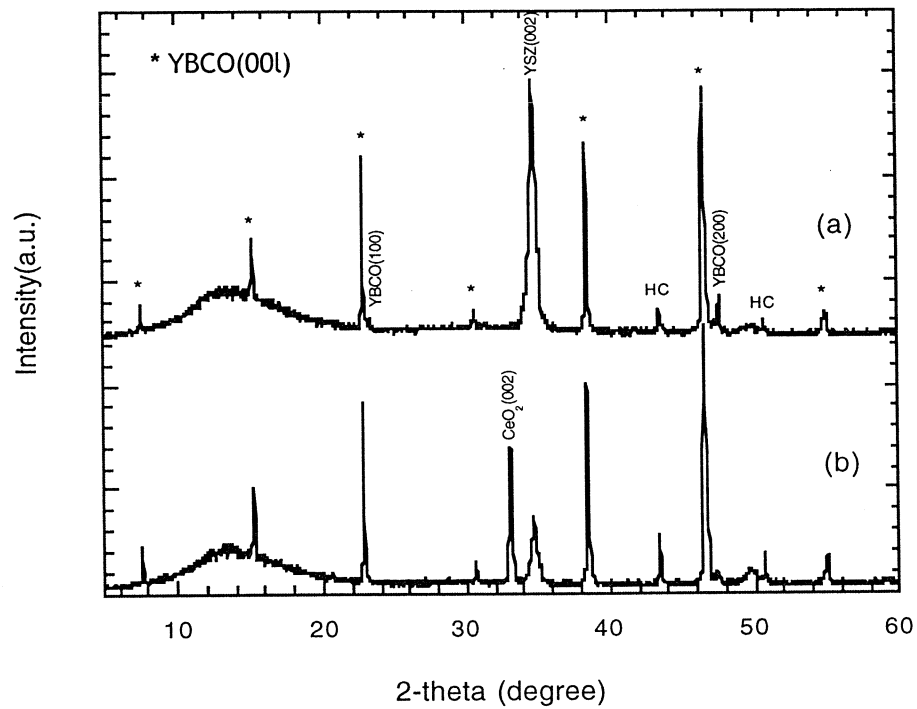


Fig. 7. XRD patterns of YBCO deposited on IBAD-YSZ-buffered HC substrates by PLD.

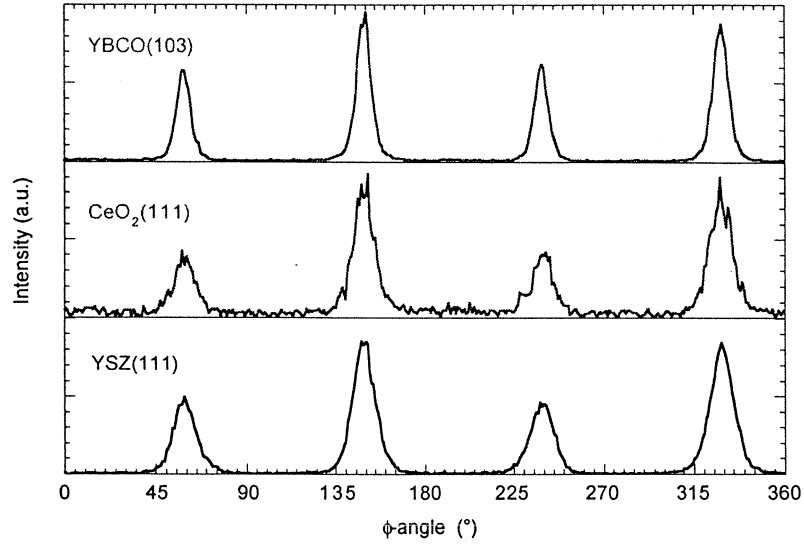


Fig. 8. X-ray  $\phi$ -scan patterns of YBCO (103),  $\text{CeO}_2$  (111), and YSZ (111), showing epitaxial growth.

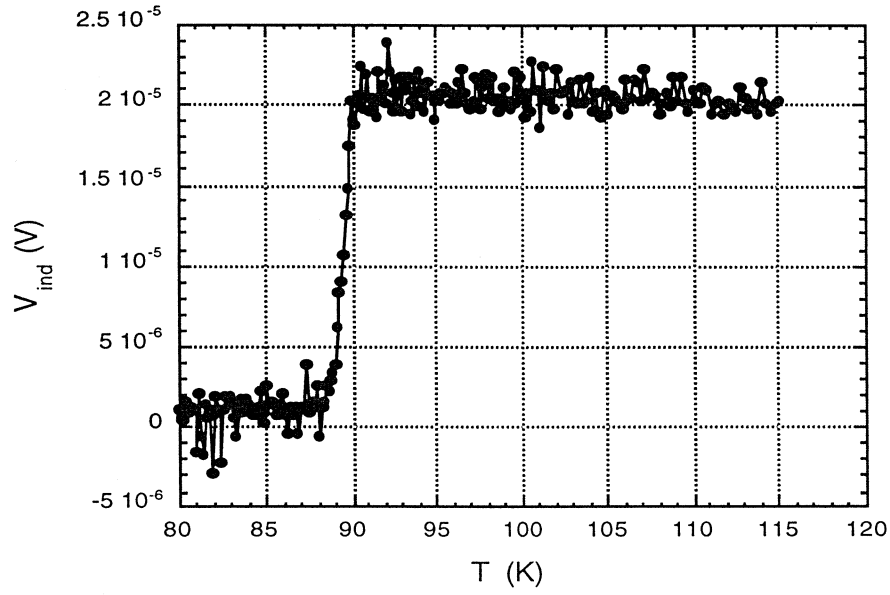


Fig. 9. Critical-temperature transition curve for YBCO film deposited on  $\text{CeO}_2$ -buffered IBAD YSZ on Hastelloy C substrate.



## Oxidation of Hastelloy C276

Depending on which thin-film technique is used to deposit the requisite buffer and superconductor layers, the alloy can be exposed, in a variety of atmospheres, to temperatures as high as nearly 800°C. We have studied the oxidation kinetics of Hastelloy C276 and the nature of the resulting oxide layer.

Hastelloy C276 foil  $\approx 0.4$  mm thick was obtained from Goodfellow (Berwyn, PA). Specimens of  $1\text{--}1.5\text{ cm}^2$  were sheared from the strip and then oxidized at 300–800°C in a flowing atmosphere, in which the oxygen partial pressure ( $p\text{O}_2$ ) ranged from 0.01% to 100%  $\text{O}_2$ /balance Ar. Weight gain was monitored by thermogravimetric analysis (TGA). X-ray diffraction and scanning electron microscopy (SEM) were conducted for each oxidized specimen. For most specimens, a diamond-stylus profilometer was used to measure surface roughness.

Both the X-ray diffraction and SEM observations revealed only the presence of  $\text{Cr}_2\text{O}_3$  in our scales. Most coupons were oxidized in the as-rolled condition. We believed initially that this condition most closely matched that of the exposed surface of our coated conductors during one-sided deposition of buffers and superconductor. The average surface roughness of an as-rolled surface was  $\approx 110$  nm, and some surface scale was present initially. The polished surfaces, on which the buffer layers and YBCO are deposited, exhibited an average roughness of  $\approx 2$  nm, which appeared to represent the effective limit of the measurement sensitivity of the profilometer.

Typical TGA data of weight gain vs. time are shown in Fig. 10; the kinetics of most traces were approximately parabolic. We therefore plotted weight gain ( $\Delta W$ ) per area ( $A$ ) vs. time ( $t$ ). Linear fits yielded values of the parabolic rate constant ( $K_p$ ) in units of  $\text{mg}^2/\text{cm}^4\cdot\text{s}$ .  $K_p$  values vs. temperature ( $T$ ) were then plotted for measurements at various  $p\text{O}_2$  values (Fig. 11). Two trends in the  $K_p$  data were clear.  $K_p$  was not a consistent function of  $p\text{O}_2$ , and no single rate constant could be ascribed to the data.

The TGA data can be converted to thickness of oxide if one assumes that the scale is  $\text{Cr}_2\text{O}_3$ . The density of  $\text{Cr}_2\text{O}_3$  was taken as  $5.225\text{ g/cm}^3$ . At all temperatures, the  $\Delta W$  data exhibited scatter with respect to  $p\text{O}_2$ . For a deposition time of 2 h, scales  $\approx 20\text{--}120$  nm thick would be expected at 755°C (Fig. 12). This thickness is commensurate with that of most of the buffer layers in our coated conductors.

The questions remain as to whether scales grown intentionally on Hastelloy C276 can be sufficiently smooth and uniform to allow for subsequent buffer deposition and whether these scales can provide any benefits in terms of, for example, impeding diffusion of cations from the substrate to the YBCO conductor.

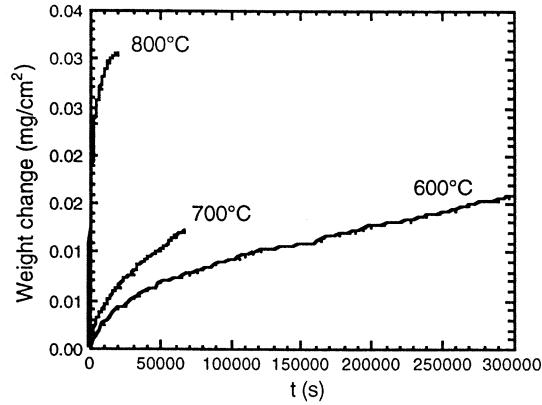


Fig. 10. Representative data for weight gain vs. time for oxidation of Hastelloy C276 in 0.01% O<sub>2</sub>.

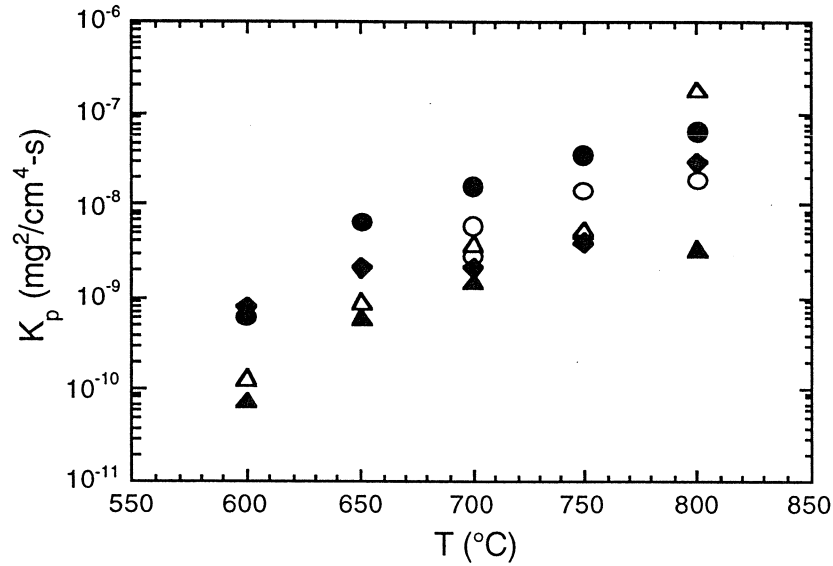


Fig. 11. Summary of parabolic rate constant vs. temperature for oxidation of Hastelloy C276 in various atmospheres: 0.01% O<sub>2</sub> (filled diamonds), 0.1% O<sub>2</sub> (open triangles), 1% O<sub>2</sub> (filled triangles), 10% O<sub>2</sub> (open circles), and 100% O<sub>2</sub> (filled circles).

Work is in progress to address these questions. Annealing at 300–800°C have yielded important information on the surface finish of the resulting scales. Within the accuracy of the profilometry measurements, it appears that annealing at 500°C produces a scale that is as smooth as the underlying metal (Fig. 13). The scales grown at temperatures  $\geq 600^\circ\text{C}$  clearly became rougher with increasing temperature. The scales grown at temperatures  $\leq 400^\circ\text{C}$  appeared to become slightly rougher with decreasing temperature.

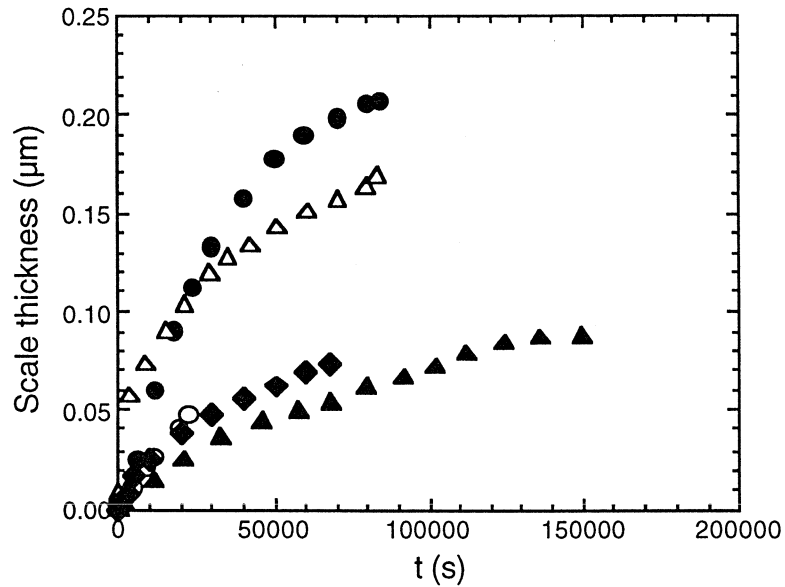


Fig. 12. Scale thickness vs. time for oxidation of Hastelloy C276 at 700°C in 0.01% O<sub>2</sub> (filled diamonds), 0.1% O<sub>2</sub> (open triangles), 1% O<sub>2</sub> (filled triangles), 10% O<sub>2</sub> (open circles), and 100% O<sub>2</sub> (filled circles).

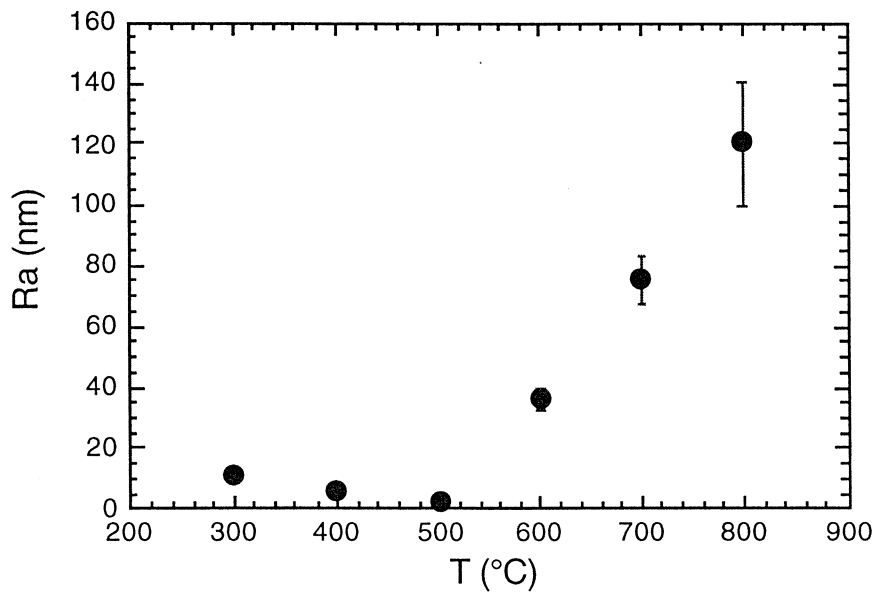


Fig. 13. Average surface roughness of scale on polished Hastelloy C276 vs. temperature for scales grown for 10 h in 100% O<sub>2</sub>; error bars are standard deviations.

Current work on oxidized Hastelloy C276 is divided into kinetics studies of polished substrates, more-detailed characterization of the resulting films, and use of oxidized substrates in fabricating coated conductors.

#### Microstructure and Properties of Internally Oxidized Ag/1.12 At.% Mg

We have reported previously on dispersion hardening of Ag-Mg alloy sheaths through internal oxidation of reactive solute species. This treatment can substantially improve strength and strain tolerance of  $\text{Bi}_2\text{Sr}_2\text{CaCu}_2\text{O}_x$  (Bi-2212) and  $(\text{Bi,Pb})_2\text{Sr}_2\text{Ca}_2\text{Cu}_3\text{O}_x$  (Bi-2223) conductors. This hardening may also allow the use of Ag-Mg alloys in coated-conductor applications. Hardening through formation of Mg-O clusters and MgO precipitates has been confirmed, and hardness increases have been documented. However, the tensile properties of hardened AgMg alloys are more relevant than hardness to wire applications. We have completed a series of studies in which the heat treatment has been correlated to tensile strength, ductility, and microstructure.

Thermogravimetric analysis (TGA) data from the Ag/1.12 at.% Mg alloy have been presented previously and published. In brief, as expected, the times to reach oxygen saturation increased with decreasing temperature. Furthermore, the oxygen saturation levels were higher at lower temperature, and the saturation reached a maximum and then decreased with increasing time at temperature. The TGA data provided evidence of an internal oxidation process that involved clustering of O and Mg species.

The presence of the inferred clusters was confirmed by TEM (Fig. 14). Uniform distributions of clusters were observed. In, for example, the sample treated at 450°C, the clusters were smaller ( $\approx 30$  Å) and more densely distributed than in the sample treated at 825°C (cluster size  $\approx 50$  Å). Observed cluster size agreed well with those predicted from the Mg/O ratios.

Tensile data provided some surprises. A representative plot of load-displacement data is shown in Fig. 15. It should be noted that the slope is not the elastic modulus because the load-train compliance was low. Exceptions to the typical brittle behavior occurred in the coupons that were saturated with O at 500°C and subsequently annealed at 825°C. Although these coupons exhibited brittle fracture after the first heat treatment, the second treatment resulted in extensive ductility (Fig. 15b). These specimens were the only ones to exhibit ductility. Average fracture stresses are shown in Fig. 16.

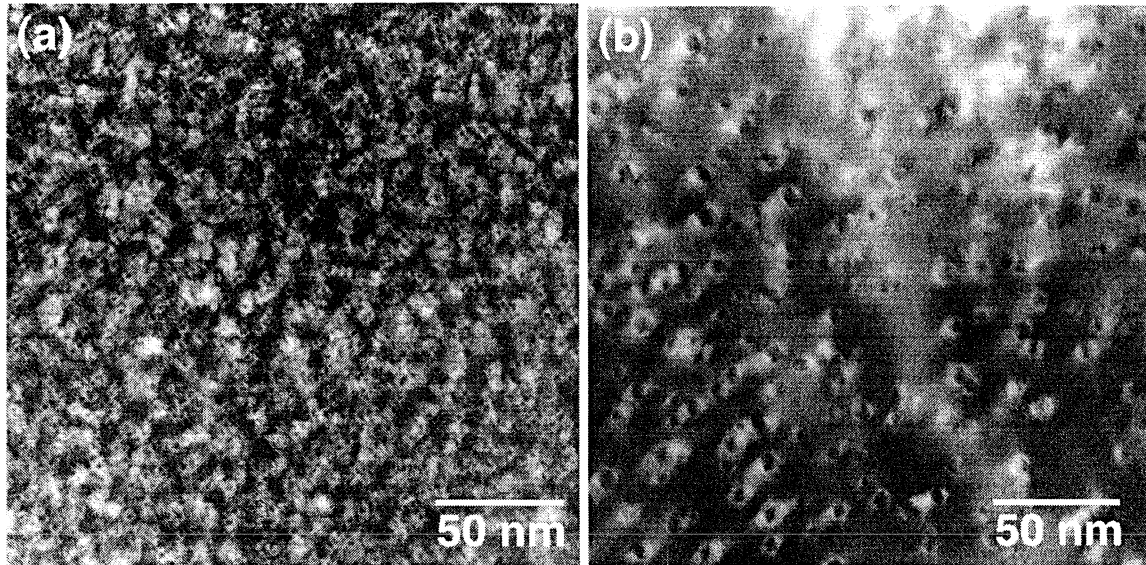


Fig. 14. Plan-view TEM images of coupons subjected to heat treatment at (a) 450 and (b) 825°C.

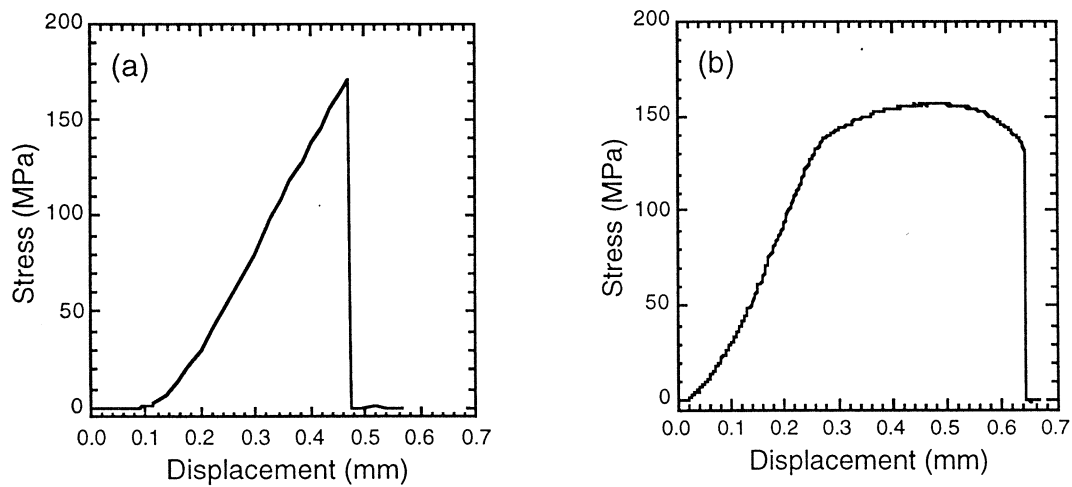


Fig. 15. Representative tensile-test data: (a) specimen saturated with O at 600°C and (b) specimen saturated with O at 500°C and then heated for 50 h at 825°C.

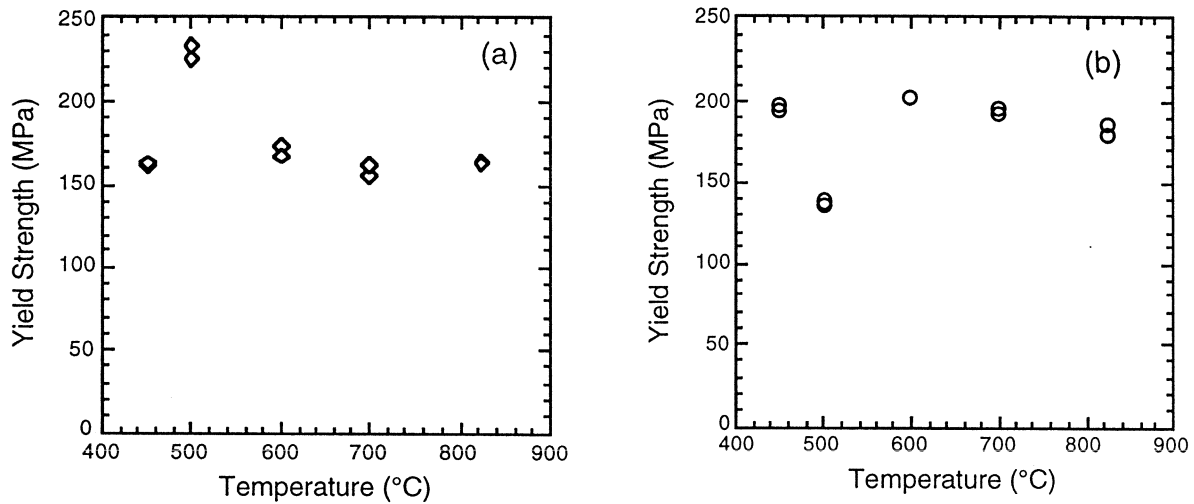


Fig. 16. Summary of tensile strengths: (a) specimens saturated with O and (b) specimens saturated at temperature shown and then heated for 50 h at 825°C.

The cause of the anomalous behavior at 500°C is not yet clear. In a kinetic analysis presented previously, a discontinuity in the parabolic rate constant for internal oxidation at temperatures below 600°C and an oxygen pressure of  $\approx 8\%$   $O_2$  was discussed. Both this discontinuity and the anomalous mechanical data could be due to a change in oxidation behavior, such as a superstoichiometric oxidation reaction of Mg or oxidation of an Ag-Mg-O intermediate phase that is stable only at 8%  $O_2$  and below 600°C. Alternatively, diffusion could possibly occur faster along dislocations in cold-worked Ag-Mg alloys internally oxidized at low temperatures.

#### Analysis of Residual Stresses

Residual strains, and hence residual stresses, develop during the processing of coated conductors as a result of differences in thermal expansion for the various layers. These stresses may cause microcracking in the superconductor layer, which may degrade its superconducting properties and reduce its service life. Therefore, it is critical to evaluate residual stresses in coated conductors and improve our understanding of the relationship between residual stresses and various processing parameters. To better understand the development of residual stresses in coated conductors, X-ray diffraction techniques are being used to measure residual stresses in the ceramic buffer and superconductor layers of simple coated conductor systems. So far, we have examined both ceramic ( $LaAlO_3$ ) and metal (Hastelloy C) substrates that were coated with YBCO superconductor or a  $ZrO_2$  buffer layer.

Using X-ray diffraction, we calculated residual strain from the measured lattice spacing  $d$  for a particular (hkl) reflection for the coating. The lattice strain ( $\epsilon$ ) associated with the (hkl) plane is given by  $\epsilon = (d - d_0) / d_0$ , where  $d_0$  is the unstrained (hkl) spacing obtained from the strain-free powder. Subsequently, stress analysis was performed and the measured strains in different directions were used to evaluate residual stresses associated with specific planes. The measured stresses were compared with calculated values of thermal mismatch stresses, and the comparison shed light on the nature of stress evolution in these coatings.

We initially evaluated the effects of processing technique on the development of residual stresses in 8 mol.% yttria-stabilized  $\text{ZrO}_2$  (YSZ) films that were deposited on Hastelloy C by ion-beam-assisted deposition (IBAD). Textured YSZ was grown at an ion-beam bombardment angle of  $\approx 55^\circ$ , while untextured YSZ of the same thickness was grown at an angle of  $\approx 67^\circ$ . Using the (200) reflection for the films, we measured compressive residual stresses of  $\approx 375$  MPa and  $\approx 600$  MPa for the textured and untextured films, respectively. Both measured stresses are much larger than the calculated thermal mismatch stress ( $\approx 125$  MPa). This large difference between the measured stresses and the calculated thermal mismatch stress is believed to result from Ar ion-peening effects during IBAD processing. Impingement of the Ar ions produced compressive stresses in both films, but channeling effects reduced ion-peening in the textured film made at  $\approx 55^\circ$ . By comparison, the ion-peening effect was larger during formation of the untextured film because there was no channeling. This leads to a greater induced internal stress and thus a higher measured residual stress in the untextured film.

In contrast to the  $\text{ZrO}_2$  films on Hastelloy, a  $\text{YBa}_2\text{Cu}_3\text{O}_{7-x}$  (YBCO) film deposited on  $\text{LaAlO}_3$  by the sol-gel technique showed good agreement between the measured residual tensile stress ( $450 \pm 80$  MPa) and the calculated value (525 MPa) of thermal mismatch stress. In this case, no internal stresses are induced due to the absence of ion-peening effects, and hence good agreement between the measured and calculated values of the residual stress is observed.

### Magnetic Diffusion in High- $T_c$ Superconductors

A potential application of high- $T_c$  superconductors for the electric power industry is the fault current limiter (FCL). A leading candidate for FCLs is the so-called superconductor-shielded core reactor (SSCR), a passive device that consists mainly of a closed iron core inside a superconductor tube and a copper coil wound on the outside of the superconductor tube [1-5]. The SSCR uses the shielding capability of a superconductor tube to keep the inductance low under normal operating conditions. Under fault conditions, the high current in the copper coil exceeds the shielding capability of the superconductor tube and there is a jump in impedance because the iron core is no longer shielded from the coil by the superconductor tube.

Originally, it was thought that the SSCR is an inductive device because the coupling between the superconductor and the primary circuit is magnetic. For some time, however, it has been realized from test results that a closed-core SSCR is really a resistive device [6]. The superconductor tube heats significantly during a fault, and its recovery is usually much longer than that of an inductive device because heat must be removed from the superconductor after the fault is cleared. An equivalent circuit of an ideal transformer, based on the lumped parameter, can be used to explain the resistive behavior of the SSCR quite well [6]. However, in general, we do not understand how the superconductor tube behaves both magnetically and thermally during a fault. In an effort to understand the behavior of a superconductor, the transient response of a superconductor tube to a pulsed magnetic field was studied experimentally [7-8]. In this report, the concept of magnetic diffusion [7,9] is used to qualitatively explain the important experimental observations on the transient response of a superconductor tube to a pulsed magnetic field.

The experimental measurements were obtained with a test section made of a copper coil wound on a cylindrical superconductor tube, as shown in Fig. 17. The copper coil had 1200 turns and was made of 0.71-mm-diameter copper wire. The material of the superconductor tube was bulk  $\text{Bi}_2\text{Sr}_2\text{CaCu}_2\text{O}_x$  (BSCCO) and was made by a melt-cast process. The BSCCO tube was 74.8 mm long, with a wall thickness of 5.5 mm and an outside diameter of 25.6 mm. A Hall probe was placed near the center of the tube to measure the magnetic field in the hole of the tube. A Rogowski coil was employed to measure the induced current in the superconductor tube. The copper coil was connected to a pulsed current source. A more detailed description of the experimental apparatus and the experimental procedure can be found in Ref. 7. Figure 18 shows the typical response of the melt-cast-processed BSCCO-2212 superconductor tube subjected to a pulsed magnetic field.

The most important feature of Fig. 18 is the time delay between the peak excitation current  $NI$  and the peak penetrated field  $H$  at the center of the tube. It can be observed from Fig. 18 that during the period from 22 to 32 ms, the magnetic field  $H$  is still increasing while the excitation current  $NI$  has already reached its peak and begun to decrease. A second important feature of the experiment is that as the peak excitation current  $NI_{\text{max}}$  is increased, the time delay between peak  $NI$  and peak  $H$  decreases. Another important feature of the experiment is that the penetration field  $H^*$  (Fig. 7 of Ref. 7) increases with peak  $NI$ . As we shall see, all three salient features of the experimental results can be explained qualitatively by the linear magnetic-diffusion model.

The geometry of the analytical model adopted here is a slab with thickness  $2a$  in the  $x$  direction, subjected to a sinusoidal applied field in the  $z$  direction, as shown in Fig. 19. The governing equation is

$$D_m (\partial^2 B / \partial x^2) = \partial B / \partial t, \quad (1)$$



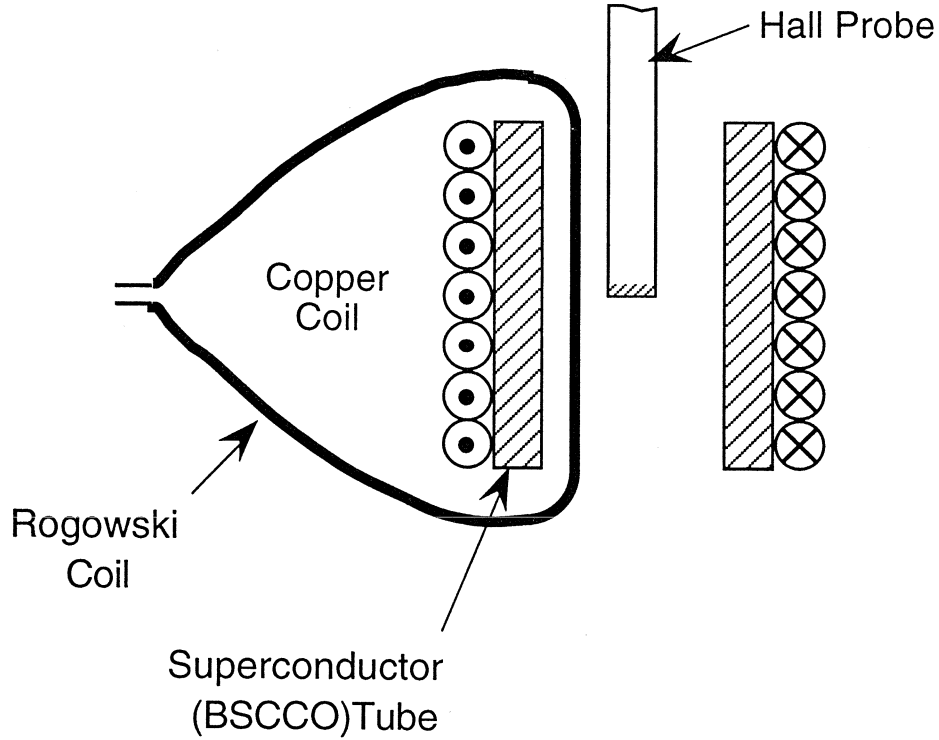


Fig. 17. Schematic diagram of apparatus used to measure the transient response of a melt-cast Bi-2212 tube to a pulsed magnetic field.

where the magnetic diffusion coefficient  $D_m$  is given by

$$D_m = \rho / \mu_o, \quad (2)$$

$\rho$  is the resistivity,  $\mu_o$  is the permeability of free space,  $B$  is the magnetic flux density in the  $z$  direction, and  $t$  is time.

Relevant parameters of the model include the characteristic length  $\delta$ , also known as the skin depth, and the characteristic time  $\tau$ . These are given by

$$\delta = (2D_m / \omega)^{1/2} \quad (3)$$

and

$$\tau = a^2 / D_m, \quad (4)$$

where  $\omega$  is the driving frequency for the applied field. A more detailed description of the model may be found in Ref. 10. The characteristic length  $\delta$  is small only if the frequency  $\omega$  is very large or if the resistivity is very small. In general,  $\delta$  can be large or small compared with the characteristic dimension  $a$  of the superconductor.

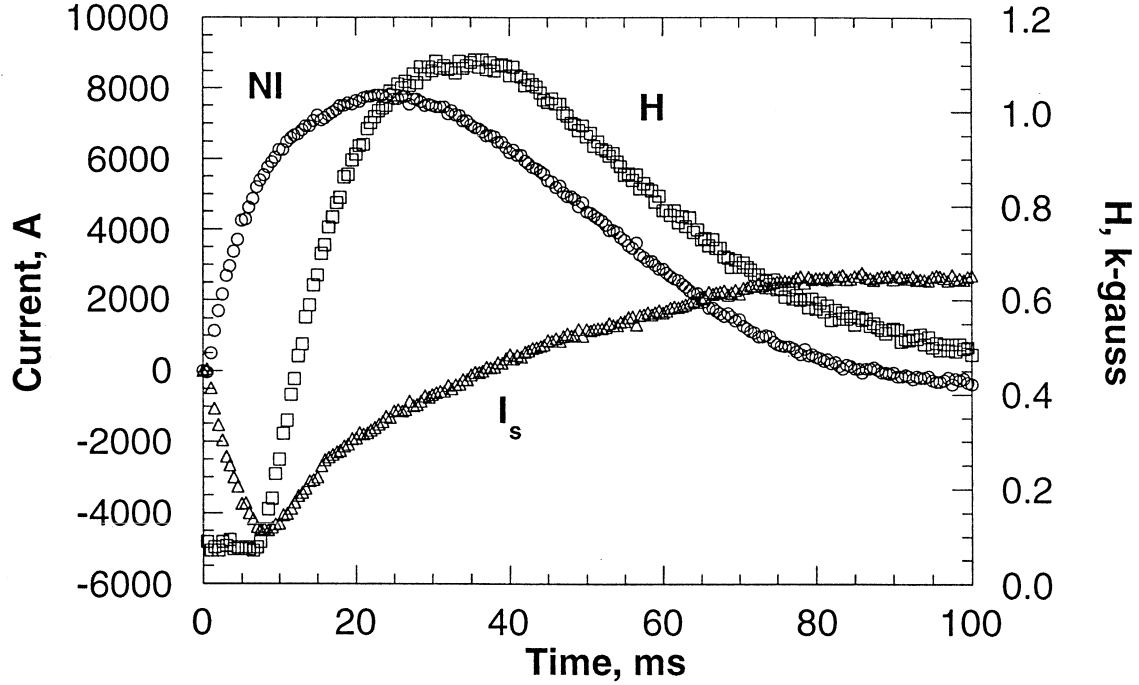


Fig. 18. Transient response of a melt-cast-processed BSCCO-2212 superconductor tube to pulsed magnetic field.  $N$  is the number of turns of the copper coil;  $NI$  is the excitation current in the copper coil;  $H$  is the magnetic field in the hole of the tube measured by a Hall probe; and  $I_s$  is the induced current in the superconductor tube, deduced from the signal of the Rogowski coil. (Adopted from Ref. 7.)

Based on the linear magnetic diffusion model, the time evolution of magnetic flux density was calculated at various locations in the superconductor along the  $x$  direction, as shown in Fig. 20 for  $a/\delta = 2$ . The horizontal axis is the time, normalized by the period  $T_0$ . For a 60-Hz AC system, the period is  $T_0 = 16.67$  ms. Briefly, the solution contains a transient term, whose decay rate depends on  $\tau$ , and a quasi-steady-state term. It can be seen that the transient dies out quickly and quasi-steady state is reached within three cycles, even for the innermost location of  $x/a = 0$ . Furthermore, it was found that the transient term modifies the quasi-steady-state solution only slightly; therefore, we will utilize the quasi-steady state solution only to explain the experimental results.

Figure 21 shows the amplitude  $A$  of the quasi-steady-state solution as a function of position for various values of  $a/\delta$ . It can be seen that the magnetic flux density is fairly uniform in the slab when  $a/\delta < 0.5$ . Very little current is induced in the slab because Ampere's law states that

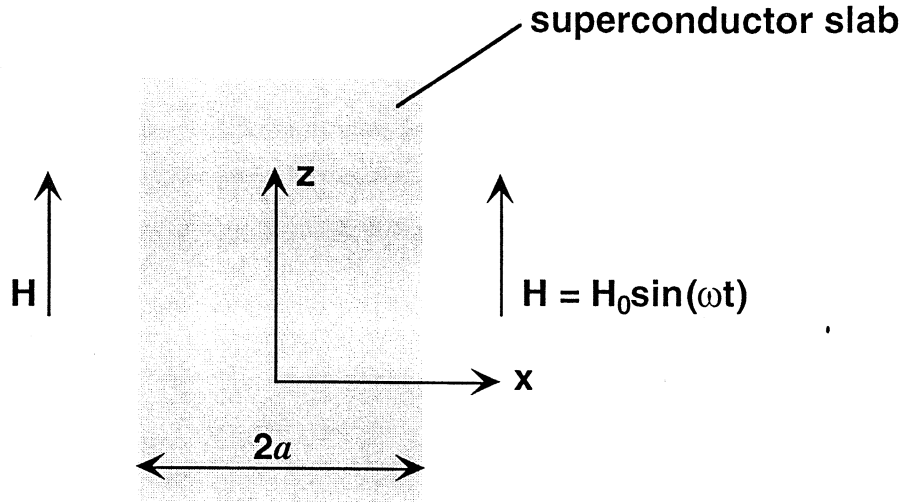


Fig. 19. Superconductor slab of thickness  $2a$  subjected to sinusoidal applied field in  $z$  direction (slab extends to infinity in both the  $y$  and the  $z$  directions).

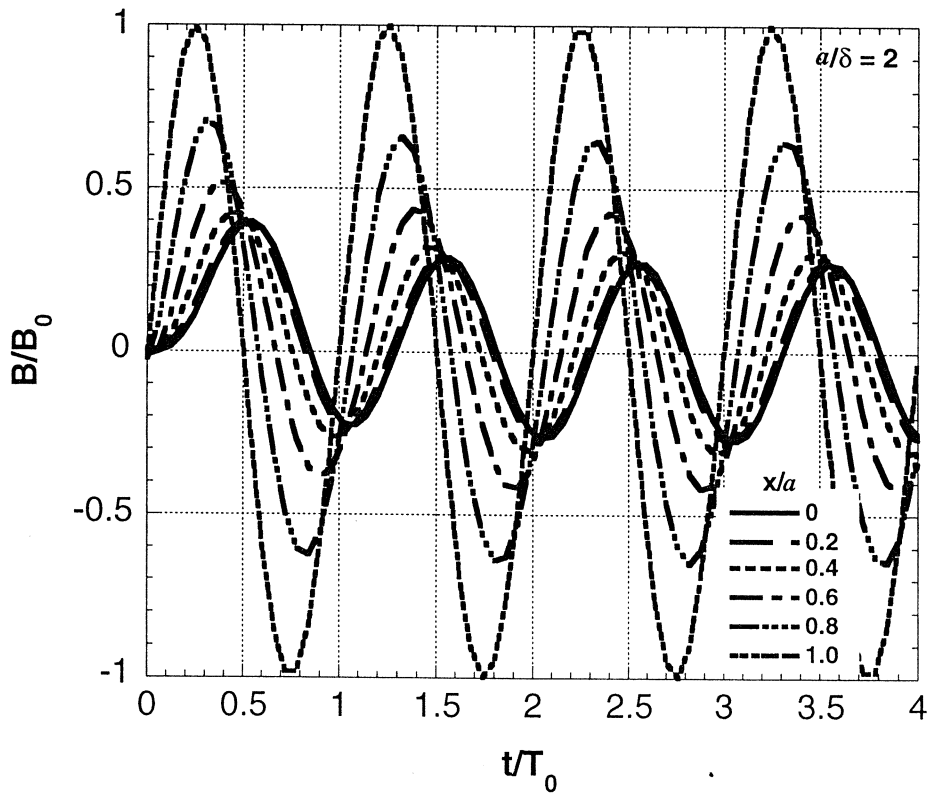


Fig. 20. Waveforms of magnetic flux density at various values of  $x/a$  in superconductor slab when  $a/\delta = 2$ .

$$\partial B / \partial x = -\mu_0 J, \quad (5)$$

which means that resistance, rather than inductance, determines the field distribution [11]. At the other extreme, the magnetic flux density is limited to a relatively thin layer near the surface when  $a/\delta > 100$ . Very high current is induced near the surface to cancel the applied field inside the bulk of the slab. In this case, macroscopic inductance, rather than resistance, is the dominant factor. Figure 21 shows that under AC steady-state conditions, the center of the slab is just penetrated by the applied field when  $a/\delta \cong 7.5$ . For  $a/\delta > 7.5$ , the magnetic flux density at  $x/a = 0$  is always zero.

To apply the linear magnetic diffusion model (Ref. 10) to the transient response of the melt-cast-processed BSCCO tube, we must keep in mind that the explanation is qualitative because the current pulse is not exactly sinusoidal, the tube is cylindrical (not a slab), and the effect of nonlinear magnetic diffusion and heating are ignored in the present model. The half-thickness  $a$  of the slab can be considered equivalent to the wall thickness of the BSCCO tube. Therefore,  $x/a = 1$  corresponds to the outside radius and  $x/a = 0$  corresponds to the inside radius of the BSCCO tube. The key parameter in the linear model is the dimensionless length  $a/\delta$ , which depends on the magnetic diffusion coefficient  $D_m$  according to Eq. 3. When  $a/\delta$  is much greater than 1, the superconductor behaves mostly like an inductor. This condition corresponds to a superconductor with a relatively low average resistivity, and only a relatively small amount of heat is generated near the outer radius of the superconductor tube. When  $a/\delta < 1$ , the superconductor behaves like a resistor; the entire wall thickness of the superconductor tube becomes resistive and the average resistivity of the superconductor is high.

Figures 22-24 show the calculated wave forms of the magnetic flux density  $B$  at various locations when  $a/\delta$  equals 0.5, 2.0, and 10, respectively. For the resistance-dominated case ( $a/\delta = 0.5$ ), Fig. 22 shows that the magnitude of  $B/B_0$  is almost the same everywhere in the superconductor because the field is fairly uniform. However, there is clearly a phase lag between peak  $B$  inside the superconductor and that at the outer surface ( $x/a = 1$ ). As  $a/\delta$  is increased to 2, Fig. 23 shows that the peak field decreases with decreasing  $x/a$ , and the phase lag between peak  $B$  inside and that at the outer surface ( $x/a = 1$ ) is greater than that shown in Fig. 22. As  $a/\delta$  is increased to 10, the time delay between the applied field and the field inside becomes even larger (Fig. 24).

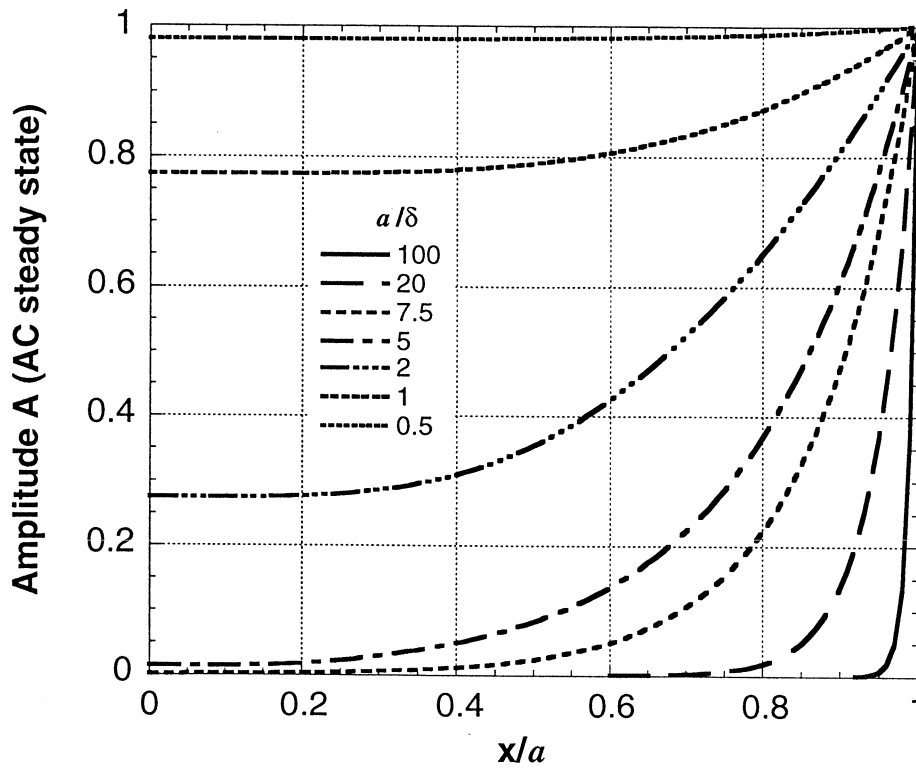


Fig. 21. Variation of amplitude  $A$  (of AC steady-state solution) with  $x/a$  for various values of  $a/\delta$ .

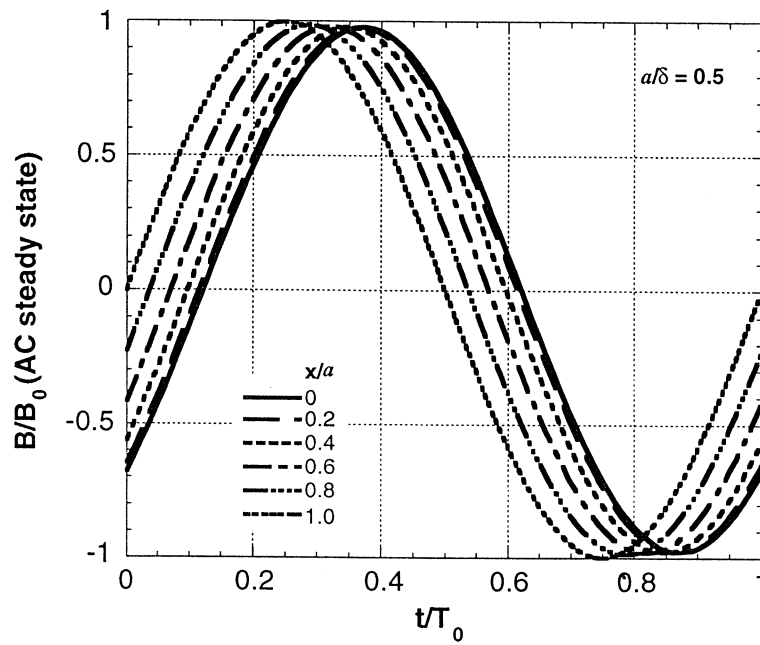


Fig. 22. AC steady-state waveform of magnetic flux density at various values of  $x/a$  when  $a/\delta = 0.5$ .

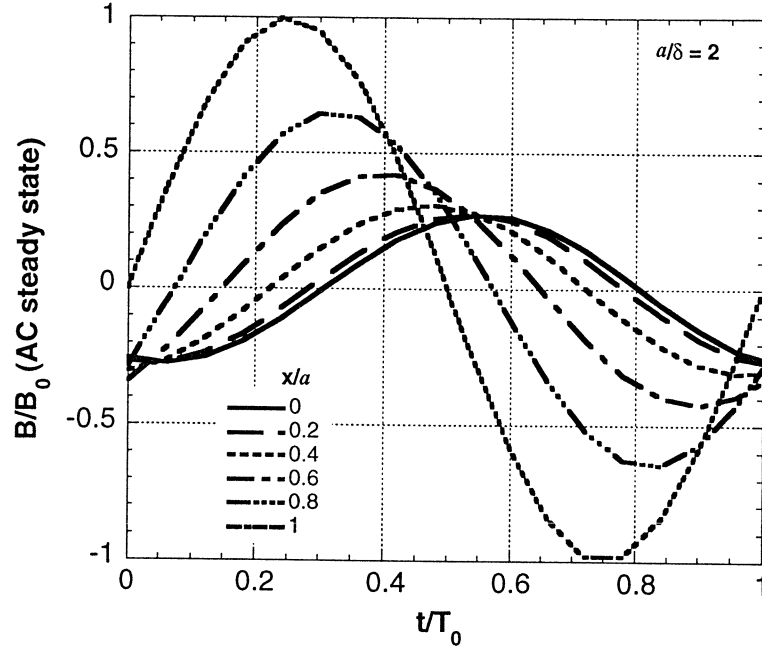


Fig. 23. AC steady-state waveform of magnetic flux density at various values of  $x/a$  when  $a/\delta = 2.0$ .

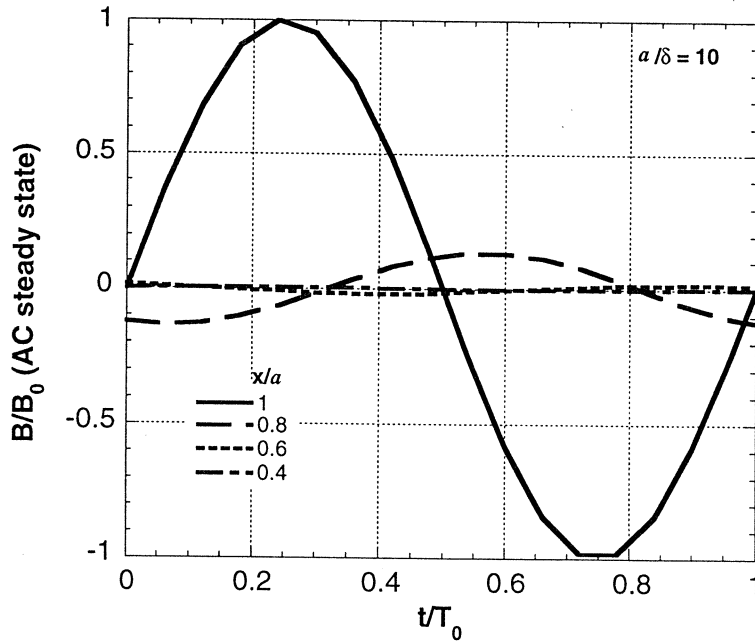


Fig. 24. AC steady-state waveform of magnetic flux density at various values of  $x/a$  when  $a/\delta = 10$ .

Figure 25 shows the calculated time delay ( $\Delta t$ ) of the peak B inside the superconductor and that at the outer surface ( $x/a = 1$ ) at various locations in the superconductor for three values of  $a/\delta$ . It clearly shows that the time delay increases with  $a/\delta$ . In other words, as the superconductor becomes more resistive, the time delay decreases. Thus, the linear magnetic diffusion model demonstrates that there is a time delay between the applied field at the outer surface ( $x/a = 1$ ) and the penetrated field at the inner surface ( $x/a = 0$ ) and this time delay decreases as the resistivity of the superconductor increases. These results agree quite well with the experimental observations described previously. Figures 22-24 also show clearly that when the applied field  $B/B_0$  (at  $x/a = 0$ ) begins to decrease after reaching its peak, the field inside the tube at  $x/a = 0$  is still rising. This finding is again in agreement with the experimental observation described previously.

A third experimental observation is that the penetration field increases with the current ramp rate. For a sinusoidal applied field, the ramp rate can be considered proportional to the angular frequency  $\omega$ . It is shown elsewhere [10] that the applied field penetrates the tube wall more readily when  $a/\delta$  is decreased. Utilizing Eq. 3, we see that

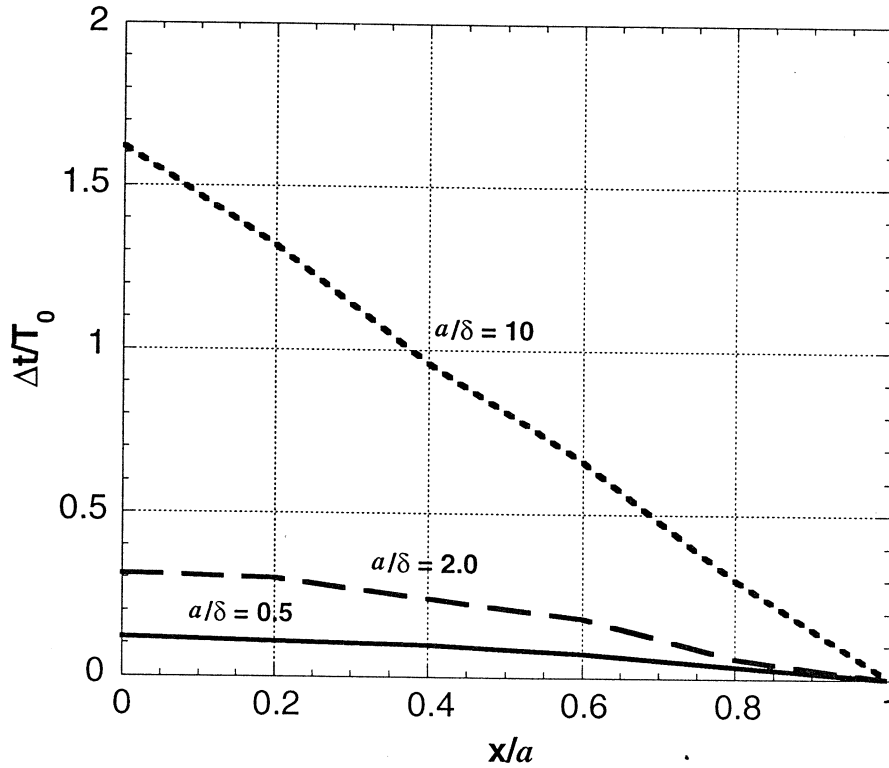


Fig. 25. Variation of time delay  $\Delta t$  (between peak B at  $x/a = 0$  and that at  $x/a = 1$ ) with  $x/a$  for various values of  $a/\delta$ .

$$a / \delta = a (\omega / 2D_m)^{1/2}. \quad (6)$$

It can be seen that  $a/\delta$  increases with  $(\omega)^{1/2}$ . When the ramp rate ( $\omega$ ) of the applied field increases,  $a/\delta$  increases, which makes penetration of the superconductor tube by the applied magnetic field more difficult. This statement is equivalent to saying that the penetration field increases with the ramp rate of the applied field. Therefore, all three salient features of the experimental observations can be explained qualitatively by the linear magnetic-diffusion model.

### Implication for Fault Current Limiters

As described earlier, a closed-core SSCR is a resistive device under fault condition and its characteristics can be explained by the equivalent circuit of an ideal transformer. An equivalent circuit is a lumped-parameter model based on linear circuit elements. It does not explain what is happening inside the superconductor tube. The field equations and the properties of the superconductor, such as flux pinning strength, govern what happens in the superconductor. As seen below, based on the results of the magnetic-diffusion model, we can explain what is happening in the superconductor tube, consistent with the lumped-parameter model of an ideal transformer.

Two experimental results that are important for the closed-core SSCR are that the device is more inductive than resistive under continuous operation at relatively low current, and it becomes resistive under fault conditions with relatively high current. At relatively low current under continuous operation, the induced current in the superconductor tube is capable of shielding the core from the external magnetic field, which means that the applied field does not penetrate the superconductor tube and corresponds to the curves in Fig. 21 when  $a/\delta > 7.5$ . This indeed corresponds to the case for an inductance-, rather than resistance-, dominated device (Ref. 11 provides an excellent account of the various limits of distributed systems). On the other hand, when the current is rapidly increasing during a fault, the superconductor tube is penetrated by the applied field and the average resistance of the superconductor increases rapidly with time. The superconductor tube is rapidly changing from an inductance-dominated system with large  $a/\delta$  ( $>112$ ) to a resistance-dominated system with small  $a/\delta$  ( $< 0.5$ ). This picture is in agreement with the experimental results of a closed-core SSCR and is consistent with the lumped-parameter model of the ideal transformer [6].

### Conclusions

It has been shown that a linear magnetic diffusion model can be used to explain the transient response of a superconductor tube to a pulsed magnetic field. The analytical results qualitatively explain the experimental observations that there is a time delay between the excitation current and the magnetic field in the core of



the superconductor tube, that the time delay decreases as the superconductor becomes more resistive, and that the penetration field increases with the ramp rate of the excitation current. Another important consequence of magnetic diffusion is that dissipation is always associated with joule heating,  $\rho J^2$ , in addition to hysteresis loss, under AC steady-state conditions. For an SSCR, the  $\rho J^2$  loss is not only important under fault conditions, but also under continuous operation, because it affects the AC steady-state critical current of the superconductor tube. The effect of magnetic diffusion on AC losses will be described more fully in a later report.

Although the linear magnetic diffusion model qualitatively explains quite well a superconductor's transient response to a pulsed magnetic field and the important electromagnetic characteristics of a closed-core SSCR, it cannot accurately predict the time evolution of the magnetic field and current distribution in the superconductor. The model has important limitations. First, as described previously, linear magnetic diffusion cannot account for flux pinning in the superconductor (nonlinear B/H curves). Second, linear magnetic diffusion is for ohmic conductors in which resistivity is constant. For high- $T_c$  superconductors, resistivity is a function of current density, magnetic field, and temperature. High- $T_c$  superconductors usually follow the so-called power law (nonlinear E/J relationship). Finally, the present treatment relates to an isothermal system in which the rate of heat generation is small and the rate of heat transfer is adequate to keep the temperature of the superconductor constant. These conditions can occur only if both the frequency and the amplitude of the applied field are small. The effects of nonlinear magnetic diffusion and heating will be discussed more completely at a later time.

## References

1. W. Paul, et al., Test of a 1.2 MVA High- $T_c$  Superconducting Fault Current Limiter, *Supercond. Sci. Technol.*, Vol. 10, 1997, pp. 914-918.
2. J. Cave, et al., Development of Inductive Fault Current Limiters Up to 100 kVA Class Using Bulk HTS materials, *IEEE Trans. Appl. Supercond.*, Vol. 9, No. 2, 1999, pp. 1335-1338.
3. V. Meerovich, et al., Performance of an Inductive Fault Current Limiter Employing BSCCO Superconducting Cylinders, *IEEE Trans. Appl. Supercond.*, Vol. 9, No. 4, 1999, pp. 4666-4676.
4. J. Nakatsugawa, et al., Magnetic Characteristics of a High- $T_c$  Superconducting Cylinder for Magnetic Shielding Type Superconducting Fault Current Limiter, *IEEE Trans. Appl. Supercond.*, Vol. 9, No. 2, 1999, pp. 1373-1376.

5. Y. S. Cha, et al., Induced Current in  $\text{Bi}_2\text{Sr}_2\text{CaCu}_2\text{O}_x$  Superconductor Tube, Appl. Supercond., Vol. 4, No. 4, 1996, pp. 173-184.
6. M. G. Ennis, T. J. Tobin, Y. S. Cha, and J. R. Hull, Fault Current Limiter - Predominantly Resistive Behavior of a BSCCO Shielded-Core Reactor, paper presented at 2000 Applied Superconductivity Conf., Sept. 17-22, 2000, Virginia Beach, VA. Manuscript submitted to IEEE Trans. Appl. Supercond.
7. Y. S. Cha and T. R. Askew, Transient Response of a High-Temperature Superconductor Tube to Pulsed Magnetic Fields, Physica C, Vol. 302, 1998, pp. 57-66.
8. Y. S. Cha, D. J. Evans, and J. R. Hull, Measurement of Critical Current and Transient Characteristics of a High-Temperature Superconductor Tube with a Pulsed Current Supply, IEEE Trans. Appl. Supercond., Vol. 9, No. 2, 1999, pp. 1320-1323.
9. Y. S. Cha, Magnetic Diffusion in High- $T_c$  Superconductors, Physica C, Vol. 330, 2000, pp. 1-8.
10. Y. S. Cha, Magnetic Diffusion and Dissipation in High- $T_c$  Superconductors Subjected to Sinusoidal Applied Fields, Physica C, Vol. 361, No. 1, Aug. 2001, pp. 1-12.
11. T. P. Orlando and K. A. Delin, Foundations of Applied Superconductivity, Chap. 2, Addison-Wesley, Reading, MA, 1991.

## Interactions

Beihai Ma and Balu Balachandran visited IGC-SuperPower during April 11-13, 2001, for technical discussions and work with IGC-SuperPower engineers to fabricate coated conductors.

Balu Balachandran attended the HTSC quarterly briefing meeting at DOE on April 19, 2001.

Balu Balachandran attended the FWP review meeting in Washington, DC on May 9, 2001.

Balu Balachandran participated in the International Superconducting Planning Meeting, Washington, DC, June 11-12, 2001.

Balu Balachandran reviewed the MicroCoating Technology program in Chamblee, GA, June 15, 2001.

Ken Gray, Beihai Ma, and Balu Balachandran attended the ISTE/C/MRS workshop in Honolulu, June 24-27, 2001.

Prof. Donglu Shi of the University of Cincinnati visited Argonne on May 5. He discussed in particular new results on sol-gel-derived YBCO films. He provided samples to Ken Goretta for microstructural characterization.

On May 21, Ken Goretta visited the Air Force Research Laboratory. He met with Dr. Timothy Peterson and discussed topics of mutual interest in coated conductors. He also met with a group of materials scientists to discuss technological challenges in fabrication of medium-sized flywheels.

### **List of Publications and Presentations**

#### Published or presented:

Y. A. Jee, B. Ma, M. Li, V. A. Maroni, B. L. Fisher, and U. Balachandran, Texture Development and Superconducting Properties of  $\text{YBa}_2\text{Cu}_3\text{O}_x$  Thin Films Prepared by a Solution Process in Low Oxygen Partial Pressure, *Supercond. Sci. Technol.* 14 (2001) 285-291.

T. M. Mulcahy, J. R. Hull, K. L. Uherka; R. A. Abboud, and J. Juna (UNICOM), Test Results of 2-kWh Flywheel Using Passive PM and HTS Bearings, *IEEE Trans. on Applied Superconductivity*, Vol. 11, No. 1, March 2001, pp. 1729-1732.

Y. S. Cha and T. R. Askew (Kalamazoo College), Transient Characteristics of a High- $T_c$  Superconductor Tube Subjected to Internal and External Magnetic Fields, *IEEE Trans. on Applied Superconductivity*, Vol. 11, No. 1, March 2001, pp. 2485-2488.

B. C. Prorok, J.-H. Park, K. C. Goretta, R. E. Koritala, U. Balachandran; and M. J. McNallan (U. of Illinois), Internally Oxidized Ag/1.2 at.% Mg Sheaths for Bi-2223 Tapes, *IEEE Trans. on Applied Superconductivity*, Vol. 11, No. 1, March 2001, pp. 3273-3276.

M. Lelovic, R. Koritala, B. L. Fisher, U. Balachandran; N. Vo, V. Selvamanickam, and P. Haldar (IGC-SuperPower), Novel Technique for Improving Field Dependence in Bi-2223 Superconducting Tapes at 77 K, *IEEE Trans. on Applied Superconductivity*, Vol. 11, No. 1, March 2001, pp. 3349-3352.

V. Selvamanickam, G. Carota, M. Funk, N. Vo, P. Haldar (IGC-SuperPower); U. Balachandran, M. Chudzik; P. Arendt, J. R. Groves, R. DePaula, and B. Newnam (LANL), High-Current Y-Ba-Cu-O-Coated Conductor Using Metal Organic Chemical-Vapor Deposition and Ion-Beam-Assisted Deposition, IEEE Trans. on Applied Superconductivity, Vol. 11, No. 1, March 2001, pp. 3379-3381.

R. E. Koritala, M. P. Chudzik, U. Balachandran, Z. P. Luo, D. J. Miller; and C. R. Kannewurf (Northwestern U.), Transmission Electron Microscopy Investigation of Texture Development in Magnesium Oxide Buffer Layers, IEEE Trans. on Applied Superconductivity, Vol. 11, No. 1, March 2001, pp. 3473-3476.

M. P. Chudzik, R. Koritala, Z. P. Luo, D. J. Miller, U. Balachandran; and C. R. Kannewurf (Northwestern U.), Mechanism and Processing Dependence of Biaxial Texture Development in Magnesium Oxide Thin Films Grown by Inclined-Substrate Deposition, IEEE Trans. on Applied Superconductivity, Vol. 11, No. 1, March 2001, pp. 3469-3472.

T. G. Truchan, M. P. Chudzik, B. L. Fisher, R. A. Erck, K. C. Goretta, and U. Balachandran, Effect of Ion-Beam Parameters on In-Plane Texture of Yttria-Stabilized Zirconia Thin Films, IEEE Trans. on Applied Superconductivity, Vol. 11, No. 1, March 2001, pp. 3485-3488.

T. R. Askew (Kalamazoo College) and Y. S. Cha, Transient Response of 50-KiloAmp YBCO Rings and Ring Pairs to Pulsed Magnetic Fields, IEEE Trans. on Applied Superconductivity, Vol. 11, No. 1, March 2001, pp. 3947-3950.

M. Li, B. Ma, Y. A. Jee, B. L. Fisher, and U. Balachandran, Characterization of Biaxially Textured YBCO Films Prepared by Pulsed Laser Deposition, Abstract presented at 103rd Ann. Mtg. of the American Ceramic Society, Indianapolis, April 22-25, 2001.

J. P. Singh and J. H. Cheon, Residual Strain/Stress Evaluation by X-ray Techniques in Buffer Layer for Coated Superconductors, Abstract presented at 103rd Ann. Mtg. of the American Ceramic Society, Indianapolis, April 22-25, 2001.

B. Ma, M. Li, Y. A. Jee, and U. Balachandran, Fabrication of Biaxially Textured Template Films by Ion-Beam-Assisted Deposition for Coated Conductor Applications, Paper presented at the 2001 Intl. Workshop on Superconductivity, Honolulu, June 24-27, 2001.

U. Balachandran, B. Ma, M. Li, B. L. Fisher, R. E. Koritala; V. Selvamanickam, G. Carota, M. Funk, N. Vo, and P. Haldar (IGC-SuperPower LLC), YBCO-Coated Conductors: Inclined Substrate Deposition and Metalorganic Chemical Vapor Deposition, Invited paper presented at the 2001 Intl. Workshop on Superconductivity, Honolulu, June 24-27, 2001.

K. E. Gray, H. Claus, Lihua Chen, B. W. Veal, A. P. Paulikas, D. J. Miller, U. Welp; R. Feenstra, and D. K. Christen (ORNL), Role of Grain Boundary Dissipation and a New Measurement Technique, Proc. 2001 Intl. Workshop on Superconductivity, Honolulu, June 24-27, 2001.

U. Balachandran, Practical Superconductor Development for Electric Power Applications, Oral presentation at the FWP Review, Washington, DC, May 9, 2001.

Submitted:

B. Ma, M. Li, Y. A. Jee, R. E. Koritala, B. L. Fisher, and U. Balachandran, Inclined-Substrate Deposition of Biaxially Textured Magnesium Oxide Thin Films for YBCO Coated Conductors, Submitted to Physica C (April 2001).

J. R. Hull and M. Komori (Kyushu Institute of Technology), High Levitation Pressures with Cage-Cooled Superconductors, Paper to be presented at 3rd Intl. Workshop on Processing and Applications of Superconducting (RE)BCO Large Grain Materials, Seattle, July 11-13, 2001.

Y. L. Tang, D. J. Miller, B. Ma, R. E. Koritala, and U. Balachandran, Structure Characteristics of YBCO Coated Conductors Based on ISD MgO Process, Abstract to be presented at MRS Fall Mtg., Boston, Nov. 26-30, 2001.

**1998-2001 Patents**

Method of Manufacturing a High Temperature Superconductor with Improved Transport Properties

Uthamalingam Balachandran, Richard Siegel, and Thomas Askew

U.S. Patent No. 6,191,075 (February 20, 2001).

Method and apparatus for measuring gravitational acceleration utilizing a high temperature superconducting bearing

John R. Hull

U.S. Patent 6,079,267 (June 27, 2000).

Engineered flux pinning centers in BSCCO, TBCCO and Y-123 superconductors  
Kenneth C. Goretta, Michael T. Lanagan, Jieguang Hu, Dean J. Miller, Suvankar Sengupta, John C. Parker, U. Balachandran, Donglu Shi, and Richard W. Siegel  
U.S. Patent 5,929,001 (July 27, 1999).

Passive fault current limiting device  
Daniel J. Evans and Yung S. Cha  
U.S. Patent 5,892,644 (April 6, 1999).

Automatic HTS force measurement instrument  
Scott T. Sanders and Ralph C. Niemann  
U.S. Patent 5,889,397 (March 30, 1999).

Method and etchant to join Ag-clad BSCCO superconducting tape  
Uthamalingam Balachandran, A. N. Iyer, and J. Y. Huang  
U.S. Patent 5,882,536 (March 16, 1999).

Elongated Bi-based superconductors made by freeze dried conducting powders  
Uthamalingam Balachandran, Milan Lelovic, and Nicholas G. Eror  
U.S. Patent 5,874,384 (Feb. 23, 1999).

Thin-film seeds for melt processing textured superconductors for practical applications  
Boyd W. Veal, Arvydas Paulikas, Uthamalingam Balachandran, and Wei Zhong  
U.S. Patent 5,869,431 (Feb. 9, 1999).

Superconductor composite  
Stephen E. Dorris, Dominick A. Burlone, and Carol W. Morgan  
U.S. Patent 5,866,515 (Feb. 2, 1999).

Surface texturing of superconductors by controlled oxygen pressure  
Nan Chen, Kenneth C. Goretta, and Stephen E. Dorris  
U.S. Patent 5,856,277 (Jan. 5, 1999).

Method for synthesizing and sinter-forging Bi-Sr-Ca-Cu-O superconducting bars  
Nan Chen, Kenneth C. Goretta, and Michael T. Lanagan  
U.S. Patent 5,821,201 (Oct. 13, 1998).

Mixed- $\mu$  superconducting bearings  
John R. Hull and Thomas M. Mulcahy  
U.S. Patent 5,722,303 (March 3, 1998).